

MEG cortical microstates: spatiotemporal characteristics, dynamic functional connectivity and stimulus-evoked responses

Luke Tait (✉ l.tait@bham.ac.uk)

University of Birmingham <https://orcid.org/0000-0002-2351-5328>

Jiaxiang Zhang

Cardiff University <https://orcid.org/0000-0002-4758-0394>

Article

Keywords: EEG microstate analysis, electrophysiology, MEG cortical microstates

Posted Date: September 7th, 2021

DOI: <https://doi.org/10.21203/rs.3.rs-842065/v1>

License:  This work is licensed under a Creative Commons Attribution 4.0 International License.

[Read Full License](#)

Version of Record: A version of this preprint was published at NeuroImage on February 1st, 2022. See the published version at <https://doi.org/10.1016/j.neuroimage.2022.119006>.

MEG cortical microstates: spatiotemporal characteristics, dynamic functional connectivity and stimulus-evoked responses

Luke Tait^{1,2*} and Jiaxiang Zhang²

¹Centre for Systems Modelling & Quantitative Biomedicine (SMQB), University of Birmingham, Birmingham, UK

²Cardiff University Brain Research Imaging Centre, Cardiff, UK

Abstract

EEG microstate analysis is an approach to study brain states and their fast transitions in healthy cognition and disease. A key limitation of conventional microstate analysis is that it must be performed at the sensor level, and therefore gives limited anatomical insight. Here, we generalise the microstate methodology to be applicable to source-reconstructed electrophysiological data. Using simulations of a neural-mass network model, we first established the validity and robustness of the proposed method. Using MEG resting-state data, we uncovered ten microstates with distinct spatial distributions of cortical activation. Multivariate pattern analysis demonstrated that source-level microstates were associated with distinct functional connectivity patterns. We further demonstrated that the occurrence probability of MEG microstates were altered by auditory stimuli, exhibiting a hyperactivity of the microstate including the auditory cortex. Our results support the use of source-level microstates as a method for investigating brain dynamic activity and connectivity at the millisecond scale.

1 Introduction

Whole-brain, non-invasive functional neuroimaging of the human brain is a useful tool for uncovering the mechanisms underpinning cognitive functions and neurological disease¹⁻⁶. In recent years, there has been much evidence that even at rest the activity of the human brain is highly dynamic, transitioning between a small number of functional brain-states with specific patterns of activation or synchrony across the cortex^{5;7-12}. These functional brain states have been associated with a range of cognitive domains and levels of consciousness^{7;13-19}, demonstrating that more advanced insight into the non-stationarity of brain states and their dynamics may be crucial to understanding cognition and disease.

In functional MRI (fMRI) data, techniques to study functional brain-states have included independent component analysis (ICA)^{7;20} and sliding-window analysis²¹, uncovering a small number of reproducible networks known as resting-state networks (RSNs)⁷. Temporal resolution of fMRI is limited by the slow dynamics of the haemodynamic response function, meaning transitions between states on a sub-second scale are likely to be missed. ICA has also been used in EEG and MEG to recreate fMRI-RSNs^{22;23}, but to do so this is typically performed on a slower time scale matching those of fMRI through analysis of downsampled power envelopes, losing the high temporal resolution and oscillatory phase information gained from the use of EEG/MEG. It follows that alternative methods are required to uncover faster time-scale (on the order of milliseconds) dynamics in EEG/MEG data¹⁰, and it is currently unclear the extent to which spatiotemporal properties of millisecond scale non-stationarity reflect those of slower RSNs.

Other methods for EEG/MEG analyses are available to examine rapid changes in brain-state. One is to apply sliding window analysis to the EEG/MEG time courses^{24–28} and subsequently cluster functional networks across windows^{21;26;29;30}. This approach has the limitation of the need for an arbitrary *a priori* selected window size: too short windows lead to results susceptible to noise, while too large windows result in non-stationarity at fast time scales being missed¹⁰. Indeed, there is no consensus on optimal sliding window length and the literature has covered a wide range, from 25ms to 30s¹⁰. A number of alternative approaches to sliding windows exist¹⁰, including Hidden Markov Models (HMMs)^{8;12}. HMMs rely on assumptions about the underlying process of state transitions, both in a detailed generative model and Markovian transitioning between states. It is unclear whether these assumptions are always met by spontaneous transitions between brain states³¹.

Another alternative approach to study dynamics of functional brain-states, the focus of the current study, is microstate analysis^{5;32}. Conventional EEG microstate analysis involves clustering the sensor-space spatial topographies using algorithms such as *k*-means or hierarchical clustering^{9;33}. Microstate analysis therefore does not require an arbitrarily chosen window length, and has minimal assumptions about the underlying generative process. Resting-state EEG microstates are robust and highly reproducible⁵, and have been associated with fMRI resting-state networks^{34–40} and cognitive domains^{13–16;18}, earning EEG microstates the nickname the ‘atoms of thought’⁴¹. EEG microstates have also been demonstrated to be a potentially useful clinical tool for understanding and diagnosing neurological diseases such as Alzheimer’s disease and other dementias^{37;42–45}, schizophrenia^{46–48}, and a range of other disorders³².

However, a key limitation of sensor-space microstate analysis is anatomical interpretation. A number of studies have attempted to reconstruct the electrophysiological sources underpinning microstates maps by combining sensor-space microstate analysis with subsequent source reconstruction^{15;45;49–52}. However, this approach may be limiting insight into functional brain states for a number of reasons. Firstly, since the inverse problem is not unique, it is possible that different spatial patterns of brain activation may give rise to similar topographical maps,

42 and therefore each sensor-level microstate may be associated with more than one active network. Secondly, due
43 to the spatial blurring in EEG as a result of volume conduction through tissues of different conductivities, EEG
44 microstate topographies have low spatial resolution and potentially cannot differentiate between finer differences
45 between maps; indeed, EEG microstate topographies are reliable with as few as eight electrodes³², suggest-
46 ing the topographies do not contain much spatial detail. Finally, since alpha band occipital sources dominate
47 the sensor-space eyes-closed resting-state EEG⁵³ likely due to head shape and the forward model resulting in
48 high signal-to-noise ratio for these regions⁵⁴, it is likely that these same sources predominantly determine the mi-
49 crostate topographies⁵², therefore suggesting the sensor-space EEG microstate maps may be under-weighting
50 the importance of non-occipital or non-alpha-band networks.

51 Instead of performing microstate analysis in sensor space and then subsequently projecting to source space,
52 here we propose first projecting M/EEG data to source space and subsequently clustering the source dynam-
53 ics. Unfortunately, some steps of the the EEG microstate pipeline means it is not directly applicable to source-
54 reconstructed recordings, such as relying the requirement to re-reference to average and being unable to account
55 (at the group level) for arbitrary source flipping. Here we adapt methodology and study microstates in MEG source
56 space at rest and during task. We hypothesise that each microstate is associated with distinct patterns of func-
57 tional connectivity across the cortex and use machine learning to test this hypothesis. Finally, we demonstrate
58 that source-space microstate features are dependent of cognitive state and examine the microstate response to
59 auditory stimuli.

60 **2 Methods**

61 **2.1 A source-space microstate pipeline**

62 The source-space microstate segmentation pipeline used here is based upon the widely used EEG sensor-space
63 k -means pipeline presented by Pascual-Marqui et al. and Koenig et al.^{55;56}, and is outlined in [Table 1](#).

64 However, there are a number of steps in the sensor-EEG microstate pipeline which limit application to source-
65 space data. One such limitation is the requirement to re-reference to average; while the EEG data itself does
66 not necessarily have to be referenced to average, the pipeline relies on metrics such as standard deviation of
67 the signal across sensors (global-field power, GFP) and correlation between spatial topographies, both of which
68 involve subtracting the mean of the map (i.e. common average re-referencing). The pipeline presented here
69 is modified, replacing standard deviations and correlations with (normalized) vector norms and cosine similarity
70 respectively. These metrics are equivalent in the case of zero mean data, and hence the methodology presented
71 here is a generalization of the sensor-EEG pipeline which may be used on reference-free data such as source
72 data or sensor MEG, while exactly preserving the EEG-microstate pipeline is under the requirement that data is

Algorithm: Source-space microstate pipeline

- 1 Source reconstruct sensor data, band-pass filter, and parcellate
- 2 Extract activity patterns (maps) at GFP peaks
- 3 Run k -means clustering on transformed (absolute value) maps.
- 4 Backfit cluster centroids to data
- 5 Calculate microstate statistics.

Table 1: **The microstate pipeline, generalized for different recording modalities.** Details and justification of these steps are given in [section 2.1](#).

73 first re-referenced to common average.

74 A second issue for source reconstructed data is that of source flipping. At the voxel level, any dipole can
 75 arbitrarily be ‘flipped’ by changing the sign of both the dipole orientation and time course. While in this study we
 76 work on the level of ROIs as opposed to individual dipoles, if parcellation is performed via a single voxel with
 77 maximal variance dipole flipping is still an issue. Another common method of parcellation (used in this study) is
 78 to take the first principal component of all dipoles within an ROI, in which case the sign of both the time course
 79 and spatial topography of the first principal component may be flipped to obtain an identical result. This source
 80 flipping is not problematic for analysis of a single M/EEG scan, but for group level analyses different participants
 81 may have different spatial patterns of source flipping. For N ROIs, source flipping can result in 2^{N-1} possible
 82 combinations. For 230 ROIs, used in this study, source flipping could result in a number of possible topographies
 83 of the order 10^{68} for a single microstate. Therefore applying traditional EEG microstate analysis to source signals
 84 may result in an overestimate of the true number of clusters in group level analysis. To confound this issue, one
 85 may use either the amplitude envelope or take the (element-wise) absolute value of the samples. The former
 86 requires a narrow band signal and rejects phase information, while the latter can be applied to broadband data
 87 and mostly maintains phase information (excluding phase differences of π). Recent work has highlighted that
 88 phase information is likely crucial for encoding microstate sequences⁵⁷. For these reasons, and based on the
 89 results of simulations ([section 3.1](#)), throughout this manuscript we use the absolute value of source estimates
 90 during clustering and map fitting.

91 A description of the source microstate pipeline are given in the following sections. While these sections give
 92 an overview the source-space pipeline, mathematical details and a generalized description of the pipeline for
 93 different modalities based appropriate modality-specific spatial transformation of the data (e.g. re-reference to
 94 average for sensor-EEG, in which case the traditional sensor-EEG microstate pipeline is recovered exactly) are
 95 given in Supplementary Text S1.

96 2.1.1 Source-reconstruction and parcellation

97 The aim of this manuscript is to present a pipeline for source-spaced M/EEG microstate analysis. The first
 98 step of the pipeline is therefore source reconstruction of the M/EEG data. A range of methodologies for source

reconstruction are currently available and the choice of methodology chosen should be data specific⁵⁸. Here, eLORETA^{59;60} was used for source-reconstruction. Full details of the pipeline for source-reconstruction in this study are given in [section 2.5.3](#). Since distributed source reconstruction methodologies typically reconstruct a large number of dipoles (several thousand), a key step following source reconstruction is spatial downsampling to increase tractability for spatial clustering. This was done through parcellation of source time courses into regions of interest. Here, the HCP230 atlas⁵⁸, a version of the Human Connectome Project's multimodal parcellation⁶¹ optimized for resting-state MEG, was chosen to reduce the source data from approximately 10,000 voxels to 230 ROI time courses. Source-reconstructed data was band-pass filtered 1-30 Hz in line with sensor-EEG microstate studies⁵.

2.1.2 Extraction of GFP peaks

Subsequently, samples with optimal signal-to-noise ratio (SNR) and topographic stability were chosen for clustering. These samples correspond to those with peaks in the global field power (GFP) (Supplementary Figure S4;^{62, 63}). In sensor-EEG microstate analysis, the GFP at a time sample t is defined as the standard deviation of the electric potential across sensors. For source-reconstructed data, the GFP is given by the vector norm of the signal across ROIs and hence is the total deviation from zero current source density (which is equivalent to the standard deviation in the case of zero mean).

Due to the 1-30 Hz bandpass filter, the GFP time course is temporally smooth, and hence local maxima of the GFP (i.e. GFP peaks) can be found using a peak-finding algorithm. Here, Matlab's `findpeaks` function was used to identify GFP peaks.

For group level analysis in this study, we randomly sampled and concatenated 5000 GFP peaks per participant. For each condition (rest/task), two MEG scans were available for each participant ($n = 30$) recorded on different dates (see [section 2.5](#)), and here we only extracted the 5000 GFP peaks from the first scan (allowing the second scan to be used for validation purposes). Hence, across participants we extracted 150,000 GFP peaks. Spatial maps at each GFP peak were submitted for k -means clustering.

2.1.3 k -means clustering

The next step of the pipeline is to cluster the submitted maps. For a given number of states, k , the algorithm for k -means clustering is outlined in [Table 2](#), while a clear graphical representation is given in Koenig et al. and Michel et al.^{56;62}.

Firstly, k maps are chosen as the initial cluster centroids. Here, the k -means++ algorithm was used for selection of initial maps⁶⁴. In the k -means algorithm, the distance between each submitted map and each centroid is calculated using the cosine distance. In the case of zero mean (e.g. such as average re-referenced

Algorithm: k-means clustering	
1	Select k maps as initial centroids
<i>While not converged:</i>	
2	Calculate distance between maps and centroids
3	Cluster each map based on nearest centroid
4	Calculate new centroids from all maps in cluster
5	Test for convergence (no change in clusters)
<i>end while</i>	

Table 2: **Outline of the k -means algorithm.**

EEG instead of source data), the cosine distance is equal to one minus correlation, which is the metric used in the sensor-EEG k -means algorithm. Each map is subsequently labelled as belonging to the state with the closest centroid. In sensor-EEG, new cluster centroids are calculated as the first principal component of all maps within the cluster⁵⁵. In source-space, new cluster centroids are calculated as the eigenvector corresponding to the largest eigenvalue of the matrix $\mathbf{Y}_j \cdot \mathbf{Y}_j^T$, where rows of the matrix \mathbf{Y}_j are the maps within cluster j . This eigenvector is equal to the first principal component in the case of zero mean. Using the new centroids, the procedure of calculating cluster labels and updating cluster centroids is iterated until convergence is reached. Due to random initial seeding, the k -means algorithm was repeated 20 times and the repetition with highest global explained variance (GEV)⁶⁵ was chosen for further analysis⁵⁶.

The choice of number of states k is a free parameter. In this study, we used the kneedle algorithm⁶⁶ to determine the optimum number of states. As the number of clusters k increases, so does the GEV. However, increasing k above the true number of states will only give marginal increases to GEV, and therefore the plot of GEV vs k has a characteristic ‘knee’ shape. The kneedle algorithm aims to find the number of clusters in the dataset by finding the value of k for which this knee occurs.

2.1.4 Backfitting to source time courses

After identifying the microstate maps from the sample of 150,000 GFP peaks, each sample of the full scan was assigned a microstate label. This backfitting was performed using previously described methods^{56:62}. Each GFP peak in the full dataset was labelled as a state based on the microstate centroid map with minimum distance. All other samples were given the same state label as their nearest GFP peak.

For each condition (rest/task), the microstate maps were extracted only from the first MEG scan, but were backfit to both scans to provide validation of microstate statistics across recording sessions.

2.2 Microstate statistics

We studied a number of spatiotemporal statistics of the resulting source MEG microstate sequences. Global statistics of the microstate sequences include GEV⁶⁵, mean duration of microstates⁶⁷, Hurst exponent of the

154 sequences⁶⁸, and microstate complexity⁴⁵. Microstate complexity values were normalized against its theoretical
155 asymptotic upper bound^{69–71}, to result in a measure $\in (0, 1]$. Class-specific statistics included mean duration of
156 the microstates within a particular class^{46;67}, coverage of a class (the percentage of time spent within a class)⁴⁶,
157 and occurrences of the class (number of times the state appears per second)⁴⁶. We also calculated the Markov
158 and syntax matrices (with and without self-transitions respectively)^{42;46;72}, the information-theoretical zeroth and
159 first order Markov statistics and their p -values⁷², and tested for non-random microstate syntax^{42;46}. Details and
160 results of analysis to quantify non-stationary, i.e. by comparing microstate statistics against random fluctuations
161 in a stationary process, are given in Supplementary Text S2.2.

162 **2.3 Microstates to study dynamic functional connectivity**

163 To derive functional connectivity for a given microstate, we adapt the EEG microstate segmented phase locking
164 method of Hatz et al.^{73;74}. The method is described in detail in Supplementary Text S1.4, and a visual overview
165 of the pipeline is given in Supplementary Figure S1. Microstate analysis was first performed on broadband (1-
166 30 Hz) data. We subsequently filtered the data into one of three narrow bands (theta 4-8 Hz, alpha 8-13 Hz,
167 beta 13-30 Hz), and calculated the Hilbert transform. For a given microstate, all samples of the analytic signal
168 within this microstate class were concatenated. Under the assumption that microstates are associated with
169 specific patterns of phase synchronization (i.e. the hypothesis we wish to test), we subsequently epoched these
170 concatenated samples into non-overlapping windows of 1280 samples (equivalent to 5-seconds), and calculated
171 phase synchronization for each window using the weighted phase lag index (wPLI)^{75;76}. wPLI was chosen
172 because it is invariant to instantaneous phase synchrony. This is advantageous in our study for two reasons.
173 Firstly, our networks will not be influenced by leakage in the inverse algorithm. Secondly, since microstate
174 analysis involves topographic clustering of the instantaneous patterns of activation, by studying only phase-
175 lagged connectivity we are not simply quantifying the same effect as microstate analysis using a different method.
176 This method was repeated for each microstate class, to obtain functional connectivity patterns for each class.

177 This methodology assumes that microstates are associated with a unique pattern of phase synchroniza-
178 tion, and therefore it is meaningful to calculate a single functional network for all samples in a given class. To
179 test this hypothesis, we applied multi-variate pattern analysis (MVPA) using the MVPA-Light toolbox⁷⁷. Across
180 all participants, resting-state scans, 1280-sample segments, and microstate classes there were 5413 networks
181 per frequency, each associated with a single microstate class. The weighted degree distributions were used as
182 features in a multi-class classifier for microstate label. Results were 5-fold cross-validated. Statistically signifi-
183 cant classification accuracy (via permutation testing) is strongly suggestive that microstates are associated with
184 unique patterns of phase synchronization, demonstrating that microstate class can be predicted given functional
185 connectivity derived from any 1280 samples from that microstate class. Details on classification are given in

186 Supplementary Text S1.4.

187 **2.4 Analysis of task microstates**

188 To compare microstates derived from resting-state and task conditions, we separately performed microstate anal-
189 ysis on data recorded from each condition and aligned microstates across conditions using a template matching
190 algorithm. Microstate statistics were averaged over all data sets available within a condition for a participant.
191 Microstate statistics between conditions were compared using paired Wilcoxon sign-rank tests.

192 To assess whether specific states were associated with auditory stimuli, we calculated an expected probability
193 of all states under the null hypothesis of no association between state likelihood and stimuli by calculating the
194 coverage of each state over samples in the pre-stimulus periods (up to 100 ms prior to the stimuli) across all
195 task scans and all participants. For a given latency in the range 0-350 ms following the stimulus, we calculated
196 an observed count of states by calculating the number of occurrences of each state over all stimuli and all
197 participants. A χ^2 test was used to compare the observed count with the expected count (equal to expected
198 probability multiplied by total number of stimuli). To post-hoc test for deviations of the count of each microstate
199 class from the expected count, we used the Pearson residual⁷⁸, calculated as

$$e_i = \frac{(O_i - E_i)}{\sqrt{E_i}}, \quad (1)$$

200 where e_i are the residuals, and O_i and E_i and the observed and expected counts of microstate i respectively.
201 The normalization by $\sqrt{E_i}$ standardizes these scores to be distributed as the standard normal distribution under
202 the null hypothesis. The χ^2 statistics can be written as $\chi^2 = \sum_i e_i^2$, and hence microstates with large magnitude
203 of e_i contribute to larger values of χ^2 .

204 **2.5 Participants and Data**

205 **2.5.1 Participants**

206 Thirty healthy participants (16 female, 9 male) were recruited from Cardiff University School of Psychology par-
207 ticipant panel (age range 17-28 years, median age 20 years). All participants had normal or corrected-to-normal
208 vision, and none reported a history of neurological or psychiatric illness. Written consent was obtained from all
209 participants. The study was approved by the Cardiff University School of Psychology Research Ethics Commit-
210 tee.

2.5.2 MEG Acquisition and preprocessing

Whole-head MEG recordings were made using a 275-channel CTF radial gradiometer system (CTF Systems, Canada) at a sampling rate of 1200 Hz. An additional 29 reference channels were recorded for noise cancellation purposes and the primary sensors were analysed as synthetic third-order gradiometers⁷⁹. One sensor was turned off during recording due to excessive sensor noise (i.e., $N_x = 274$ gradiometers). Horizontal and vertical electro-oculograms (EOG) were recorded to monitor blinks and eye movements. The horizontal electrodes were placed on temples, and vertical ones, above and below the eye. For MEG/MRI co-registration, the head shape with the position of the coils was digitised using a Polhemus FASTRAK (Colchester, Vermont).

MEG was recorded over two sessions, recorded on separate days (1-24 days between sessions). In each session, eight minutes of continuous resting-state was recorded, for which participants were instructed to sit comfortably in the MEG chair while their head was supported with a chin rest and with eyes open focus on a fixation point on a grey background. Additionally, ten minutes of passive task activity was recorded in each session, for which participants were instructed to watch an emotionally neutral movie while periodic auditory stimuli (separated by 500 ms) were played through headphones. Half of the stimuli consisted of standard tones, while the other half were a mixture of duration, gap, direction, intensity, and frequency deviates.

For preprocessing, MEG data was imported to Fieldtrip⁸⁰, bandpass filtered at 1-100 Hz (4th order two-pass Butterworth filter), notch filtered at 50 and 100 Hz to remove line noise, and downsampled to 256 Hz. Visual and cardiac artifacts were removed using ICA decomposition (aided by EOG recordings), using the 'fastica' algorithm⁸¹. For both task and resting-state data, between 2 and 6 components were removed per scan (median 4 for rest, 3.5 for task).

2.5.3 Source reconstruction

All participants also underwent a whole-brain MRI scan on a Siemens 3T Connectom MRI scanner and a 32-channel receiver head coil (Siemens Medical Systems). We used a T1-weighted magnetization prepared rapid gradient echo sequence (MPRAGE; echo time: 3.06 ms; repetition time: 2250 ms sequence, flip angle: 9°, field-of-view: = 256 × 256 mm, acquisition matrix: 256 × 256, voxel size: 1 × 1 × 1 mm).

From the T1-weighted MRI image, extraction of the scalp, brain, and cortical surfaces was performed with Freesurfer⁸². Vertices of the cortical surface were labelled according to the HCP230 atlas optimized for MEG studies⁵⁸. The scalp surface was used to align the structural data with the MEG digitizers. A single shell volume conduction model⁸³ was constructed in Fieldtrip using the brain surface (downsampled to 500 vertices). The cortical mesh was downsampled to approximately 10,000 vertices to generate a set of dipole locations using the 'iso2mesh' software⁸⁴, and dipoles were oriented normal to the cortical surface^{85;86}.

Source reconstruction used the eLORETA algorithm^{59;60} implemented in Fieldtrip. Source data was parcel-

lated using the HCP230 atlas labels⁵⁸ by taking the time course of the first principal component of all voxels with an ROI. Source time courses were bandpass filtered in the 1-30 Hz frequency band, and head localization coils were used for offline head motion correction⁸⁷.

2.6 Simulations

Simulations were performed to test the ability of the microstate methodology to estimate a ground truth microstate sequence and spatial maps, and compare modified against other methodologies for neural state identification such as PCA, ICA⁸¹, and hidden Markov modelling⁸⁸. Details of the simulations and settings for other algorithms are given in Supplementary Text S1.3. Artificial generative sequences were generated using a random walk decision tree approach, detailed in Supplementary Text S1.3, which reverse engineers a method to transform microstates to random walks^{33;68;89}. Neural dynamics were then generated by assigning each microstate a Wilson-Cowan neural mass model of resting-state dynamics^{90;91}, and stimulating the oscillator associated to the active state. Finally, the states were assigned spatial maps of the same spatial dimensionality as our data, i.e. 230 ROIs. The choice of spatial map is arbitrary, so to increase neurophysiological realism we used open access resting-state networks derived from fMRI⁷ aligned to our brain atlas. ROI time series were generated as a combination of a linear projection of each microstate's neural dynamics onto the microstate maps and pink noise with SNR=1. Twenty repetitions of the simulations were performed, and simulations were repeated for $k = 4$ and $k = 10$ states. Four statistics were used to assess the quality of the microstate estimation against the ground truth, namely GEV, map similarity, temporal mutual information (MI) the ground truth and estimated sequence, and the normalized mutual information only at the GFP peaks (MIg).

It should be highlighted that these simulations do not aim to reproduce biophysical mechanisms of microstate generation as currently these mechanisms are not well understood. Due to this, some key properties of true microstate sequences such as spontaneous transitioning and associations between GFP and state stability⁶³ are not recreated by our model. However, this should not crucially alter the outcome of our results, since the aim of the simulations was to generate artificial data with few underlying model assumptions and known ground truth maps/sequences.

2.7 Data and Code Availability

Data preprocessing and source reconstruction used Fieldtrip version 2019-07-16⁸⁰. Code for performing microstate analysis in sensor- or source-space MEG/EEG, simulations as described in this manuscript, statistics and visualisation have been compiled in the +microstate toolbox⁹² (<https://plus-microstate.github.io>), a freely-available open-source toolbox written in MATLAB R2017b. Data used in this study are available upon request.

3 Results

3.1 Simulations

We used a neural-mass model to generate synthetic time courses of electrophysiological data with a known number of microstates. The simulations were then used to test the k -means microstate algorithm against the ground truth, and to compare the performance against using PCA, ICA, and HMM for estimating brain states (see Supplementary Text S1.3.1 for a description of the methods). Figure 1 shows the simulation pipeline and results of analysing the simulated datasets. Results of GEV, map similarity, and mutual information analyses were largely consistent between simulations of 4 microstates and 10 microstates. In terms of GEV (Figure 1D), the three highest performing methodologies were k -means applied to amplitude envelopes, HMM applied to amplitude envelopes, and k -means applied to source time courses. The remaining algorithms - PCA, ICA, and source HMM - performed notably worse.

k -means and PCA most accurately recreated the ground truth maps in both source and amplitude domains, with k -means consistently outperforming PCA in all conditions except 4-state amplitude envelopes (Figure 1E). In terms of mutual information between ground truth and estimated sequences, the same two algorithms were also the highest performing (Figure 1F-G). In all conditions, source data outperformed amplitude data. Interestingly, the HMM had normalized MI of less than 5% for all simulations over all conditions (full data or GFP peaks, and amplitude or source), so performed poorly at recreating the ground truth sequences. As a consequence of these results, we used the source data as opposed to amplitude envelope data for all subsequent microstate analysis.

3.2 Resting-state microstate maps

We source-reconstructed MEG resting-state data from 30 participants. Across all participants, microstates in resting-state data were calculated from a sample of 150,000 GFP peaks using the k -means clustering algorithm. Figure 2A shows the GEV across these 150,000 peaks as k is varied from 2-40 states. The kneedle algorithm indicated that 10 states were optimum, and hence we proceeded to back-fit the results of the 10-state clustering to the full MEG scans. Figure 2B shows the GEV in the full datasets. In the first set of scans, from which the GFP peaks were sampled to estimate microstates, 10 states had a GEV of $63.97 \pm 0.64\%$. To ensure the states were generalizable and reproducible, we also back-fit the maps to a second independent scan from each participant, which was performed on a separate day and not used in the clustering analysis. There was a significant but small decrease in GEV in the second scan ($62.13 \pm 0.39\%$, $p = 0.0082$, Wilcoxon sign-rank test), as expected in cross-validation. Furthermore, multiple runs of the algorithm demonstrated high reproducibility (Supplementary Text S2.1).

Figure 2C shows the spatial map of each empirical MEG source-level microstate. Four bilateral maps were

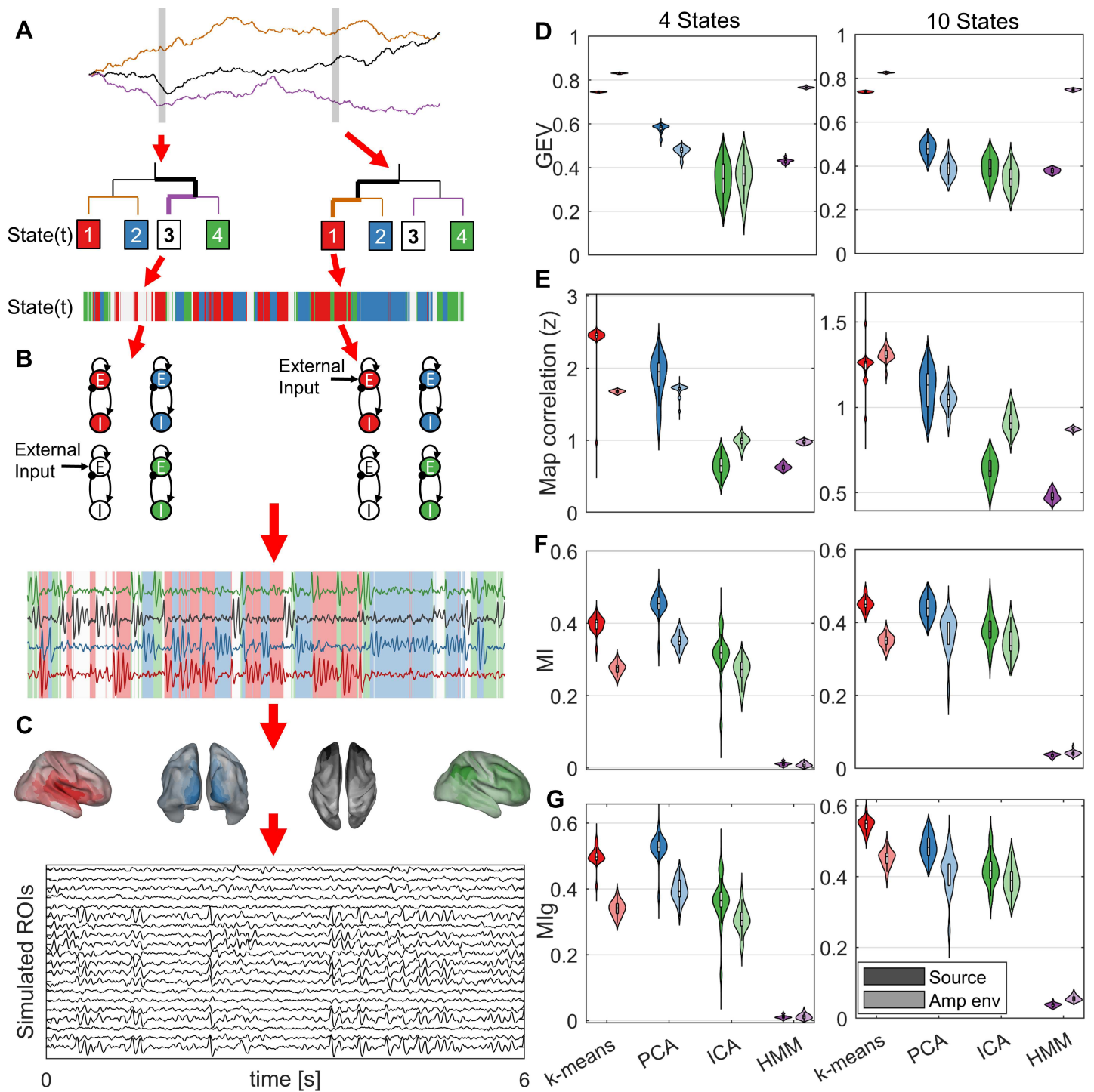


Figure 1: Simulating microstates. (A-C) Methodology for simulating microstates. Detailed description is given in Supplementary Text S1.3. (A) Generative sequences are simulated using a decision tree, the state at a given time (bottom; colours correspond to state) is decided by a set of random-walks (top) and a decision tree (middle). Colours of branches on the decision tree correspond to the colours of the random walks. The left branch is chosen if the walk is increasing, the right branch is chosen if the walk is decreasing. (Bottom) Each sample is assigned a state using this procedure. (B) Neural dynamics of microstates are simulated by assigning each state an neural mass model (NMM). The NMMs receive constant input (P) at all times, and the NMM corresponding to the current active state receives additional input (P_{ms}). The bottom shows simulated state time series, with background colour corresponding to active state. (C) Each state is assigned a spatial map and the time courses are linearly mixed according to this map to generate simulated MEG/EEG/source data. Pink noise is added to this data. (D-G) Assessment of microstate sequences estimated from simulated data vs ground truth. (D) GEV, (E) correlation between estimated maps and ground truth maps, (F) mutual information between estimated sequences and ground truth sequences.

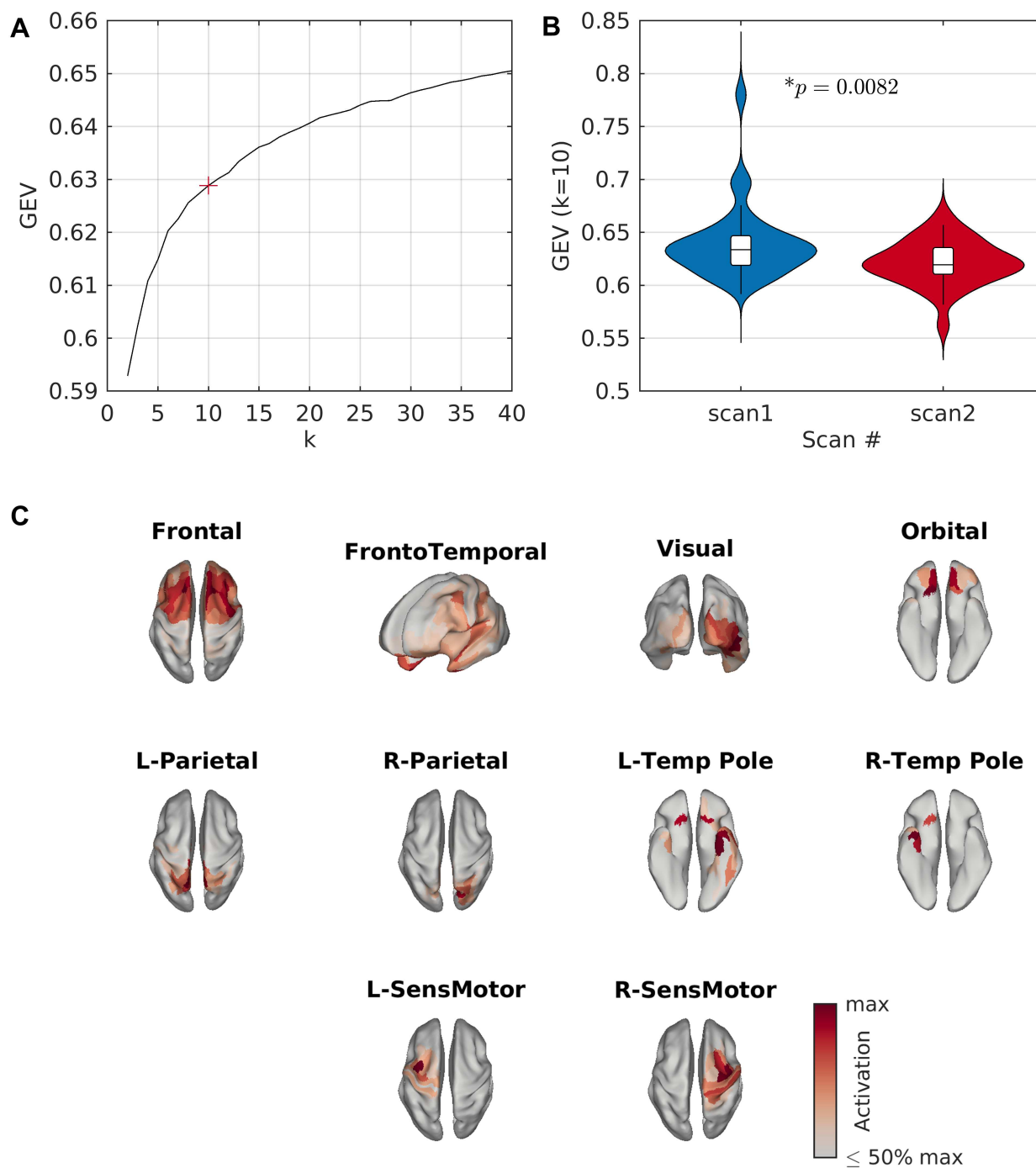


Figure 2: **Resting-state microstates.** (A) GEV vs number of states (k) for resting-state data. Here, GEV is calculated across the 150,000 peaks used for clustering. The kneedle algorithm found that $k = 10$ states was optimum, marked by a red '+'. (B) GEV across the full MEG scans, for $k = 10$. Distributions are shown across participants. Only GFP peaks from scan 1 for each participant were used for clustering, and hence scan 2 can be viewed as a replication/validation cohort. There is a small but significant decrease in GEV for scan 2. (C) Resting-state microstate maps derived from the k -means clustering algorithm for $k = 10$ states.

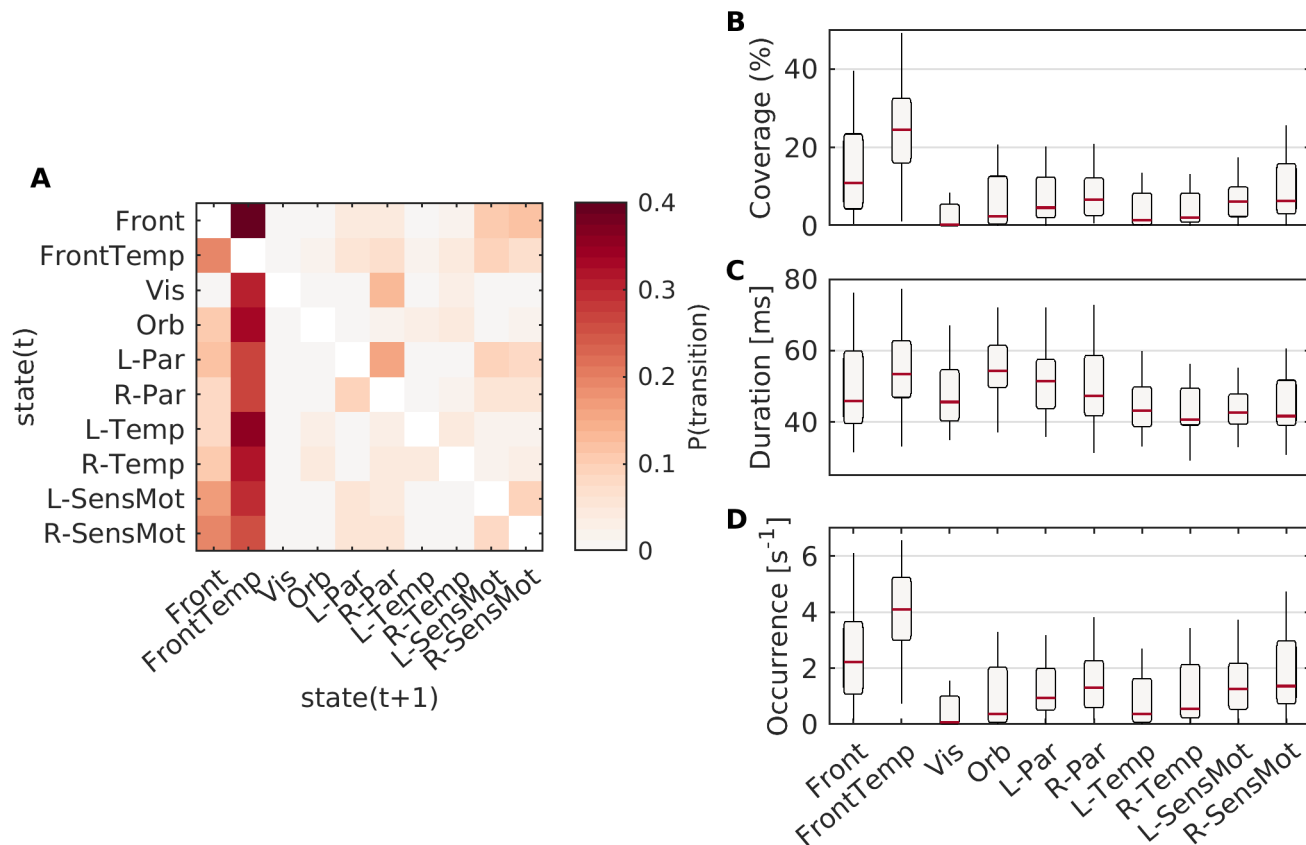


Figure 3: **Syntax of resting-state microstates.** (A) The average syntax matrix from resting-state data. (B-D) Coverage, duration, and occurrence of each of the ten resting-state microstate maps.

305 identified, including the frontal cortices, the fronto-temporal network, the visual cortex, and the orbital cortex. The
 306 remaining six maps could be grouped into three pairs of lateralized networks including medial/superior parietal,
 307 temporal poles, and sensorimotor networks.

308 3.3 Statistics of resting-state microstate sequences

309 We subsequently analysed the statistics of the estimated microstate sequences, reported in full in Supplementary
 310 Table S3. Microstates had a mean duration (MD) across all classes of 59.86 ± 1.09 ms (Supplementary Table
 311 S3). This was significantly longer than could be explained by random fluctuations in a stationary Gaussian
 312 process with the same power spectra, cross-spectra (and covariances), and distribution of data (Supplementary
 313 Text S2.2), suggestive of non-stationarity and the existence of stable microstates in empirical resting-state MEG.
 314 Durations of each state individually are shown in [Figure 3](#).

315 Of the 10 microstates, the frontal and frontotemporal states had the highest coverage and highest number of
 316 occurrences per second ([Figure 3](#)). This can be observed in the group-level syntax matrix ([Figure 3A](#)), in which
 317 almost all states tend to transition most predominantly to the frontotemporal state, which in turn is most likely to
 318 transition to the frontal state. However, random sampling of states with heterogeneous occurrences per second is

Band	Accuracy	<i>p</i> -value
Theta	0.2068 ± 0.0084	< 10 ⁻³
Alpha	0.3281 ± 0.0120	< 10 ⁻³
Beta	0.3083 ± 0.0112	< 10 ⁻³

Table 3: **MVPA classification statistics for microstate-segmented connectivity.** Accuracy is given as a mean and standard error across five repetitions.

not sufficient to explain the syntax matrix, as the syntax permutation test⁴⁶ demonstrated significant differences between the group level matrix and the matrix expected due to state probability ($p = 4 \times 10^{-4}$). Similarly, when accounting for duration and coverage (i.e. including self transitions in the Markov matrix), information theoretical analysis still demonstrated that the zero'th order Markov (G_0) property was, for all participants, far greater than expected under the null hypothesis of random sampling based on coverage of states (Supplementary Table S3). The transitioning matrix could also not be explained by a first order Markov process, as demonstrated by the Markov G_1 information theoretical analysis (Supplementary Table S3). Combined, these results suggest structured and non-Markovian transitioning in the microstate sequence.

The structured, non-stationary and non-Markovian nature of microstate transitions was additionally supported by global statistics. The Hurst exponent (H) was approximately 0.68 ± 0.01 , suggestive of long range temporal correlations. The normalized microstate complexity (C) was 0.60 ± 0.01 , suggesting a complex sequence which strikes a balance between highly repetitive and ordered (C approaching zero) and random sampling (C approaching one). These global statistics were significantly different than expected from random fluctuations in a stationary process (Supplementary Text S2.2), further evidencing the non-stationary nature of resting-state MEG.

3.4 Microstate-specific functional connectivity

Our next aim was to test the hypothesis that different microstate classes are associated with distinct patterns of functional connectivity in the brain, and reflect the rapid transitioning in dynamic phase synchronization patterns. To do so, we used multi-class MVPA to test whether microstates could be predicted from microstate-segmented wPLI connectivity matrices (see section 2.3). Table 3 shows the classification accuracy and permutation testing *p*-values for each frequency band, while Figure 4A shows the confusion matrices for this classification.

The classification accuracy was significantly above the chance level of 10% ($p < 10^{-3}$, 1,000 permutation tests from 1,000 surrogates), suggesting distinct functional connectivity patterns among microstates. The confusion matrices demonstrate interesting patterns. In the alpha and beta bands, the visual microstate is the one most accurately predicted by the connectivity matrix, while in theta the temporal microstates were more accurate. Unsurprisingly because of their overlap, frontal, frontotemporal, and orbital networks had reasonable degrees of confusion in all bands. In the alpha band, the frontal network was also sometimes confused with bilateral sensorimotor networks.

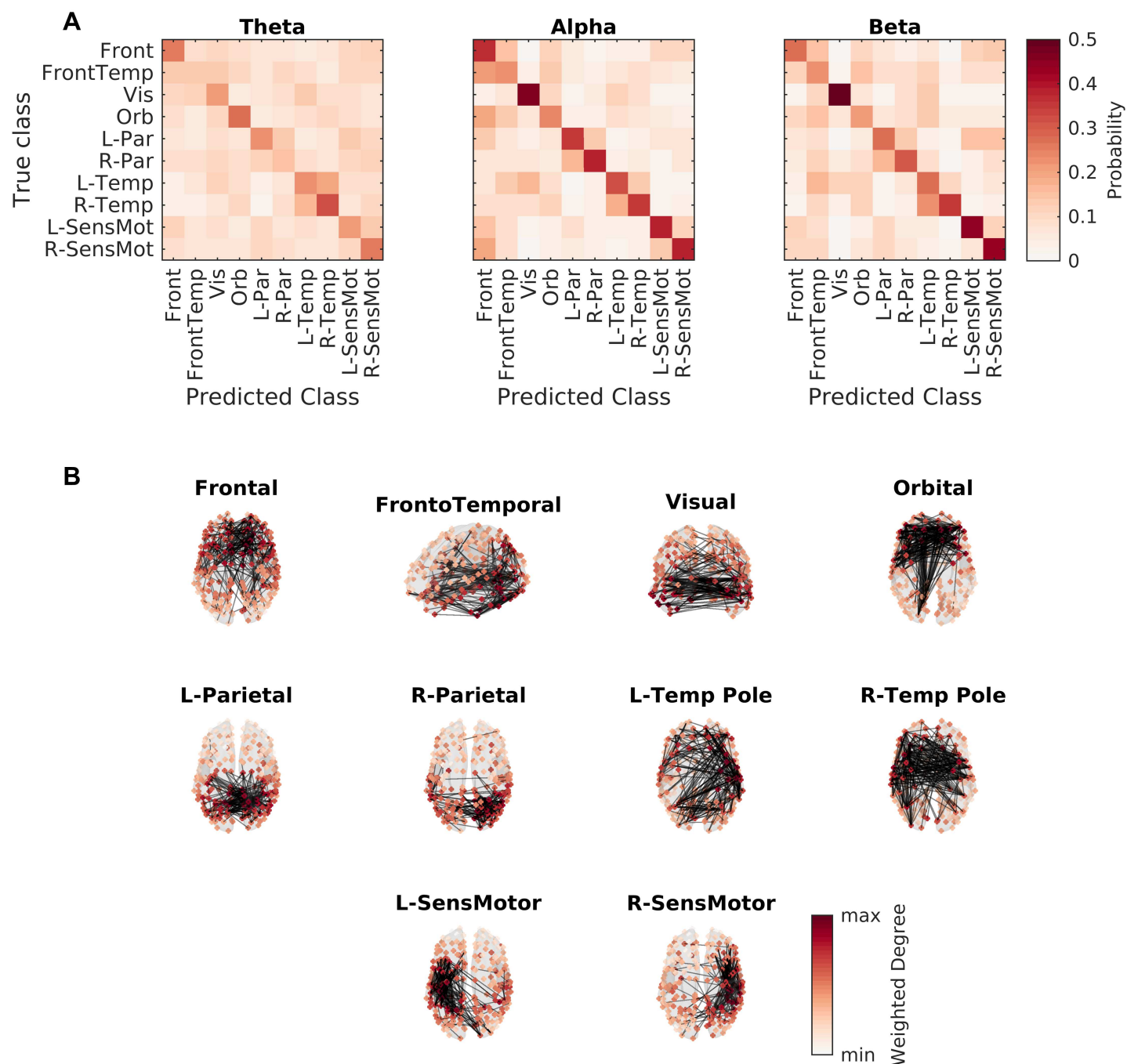


Figure 4: **Microstates are associated with specific patterns of phase synchronization.** (A) Confusion matrices for the MVPA analysis, for three frequency bands used for functional connectivity calculation. Cell i, j corresponds to the probability the classifier would predict class j given a microstate label i . (B) Functional connectivity patterns. Node colours show degree distributions (used for classification in the MVPA analysis), while edges show the top 1% of edges that deviate from static background connectivity (see Supplementary Text S1.4 for details).

346 Furthermore, lateralized microstates were regularly confused with their counterparts in the opposite hemi-
347 sphere, suggesting that while activation patterns in these states may be lateralized, the states are parts of a
348 larger interhemispherical network. Indeed, Figure 4B shows the alpha band network structures, and it is clear
349 that the functional connectivity structure for both lateralized parietal and temporal microstates demonstrated many
350 interhemispherical connections.

351 3.5 Microstates of auditory evoked response

352 Finally, we aimed to test whether source-level MEG microstates vary between rest and task. To do so, we re-
353 ran the microstate clustering analysis on MEG data during a passive auditory task. The optimum number of
354 microstates in the task data was $k = 9$. This was one fewer than at rest, yet there were no significant differences
355 in the GEV between nine states in task and ten states at rest (Figure 5A-B; $p = 0.9099$).

356 Maps for the nine states derived from the task data are shown in Figure 5C. The task-based states closely
357 corresponded to those from rest. The two lateralized medial parietal states in the resting-state data were repre-
358 sented by a single medial parietal state in the task data, explaining the presence of one fewer state. The frontal
359 and visual states demonstrated differences between conditions, with the frontal state appearing more right lat-
360 eralized and the visual state having greater spatial extent. All other states closely recreated their resting-state
361 counterparts. There were no significant differences in global statistics of the microstate sequences between rest
362 and task, including mean duration ($p = 0.5170$), Hurst exponent ($p = 0.2452$), or complexity ($p = 0.8774$).

363 To uncover whether any states were time-locked to auditory stimuli, we used χ^2 tests to compare pre-stimulus
364 and post-stimulus coverage of each state. The time evolution of χ^2 is shown in Figure 6A. There is a significant
365 difference in the observed and expected microstate counts between 70 and 280 ms following the stimulus, peak-
366 ing at 113 ms. This is in line with the auditory N100 evoked response. The differences in microstate count are
367 largely driven by a significantly increased coverage of the frontotemporal state, with resulting decreased coverage
368 of several other microstates including a significantly decreased coverage of the medial parietal state (Figure 6B).
369 Since the frontotemporal state includes the auditory network (Figure 5C), these results are in line with increased
370 activation of the auditory network as a response to an auditory stimulus.

371 4 Discussion

372 Understanding the mechanisms underpinning discrete brain state generation is currently a leading question in the
373 field of neuroscience, which may aid with understanding behaviour and cognition⁴ and neurological diseases⁹.
374 One approach to do this in sensor EEG is microstate analysis⁵, but this approach cannot be directly applied to
375 source data. In this study, we have presented a modified source-space microstate pipeline and demonstrated

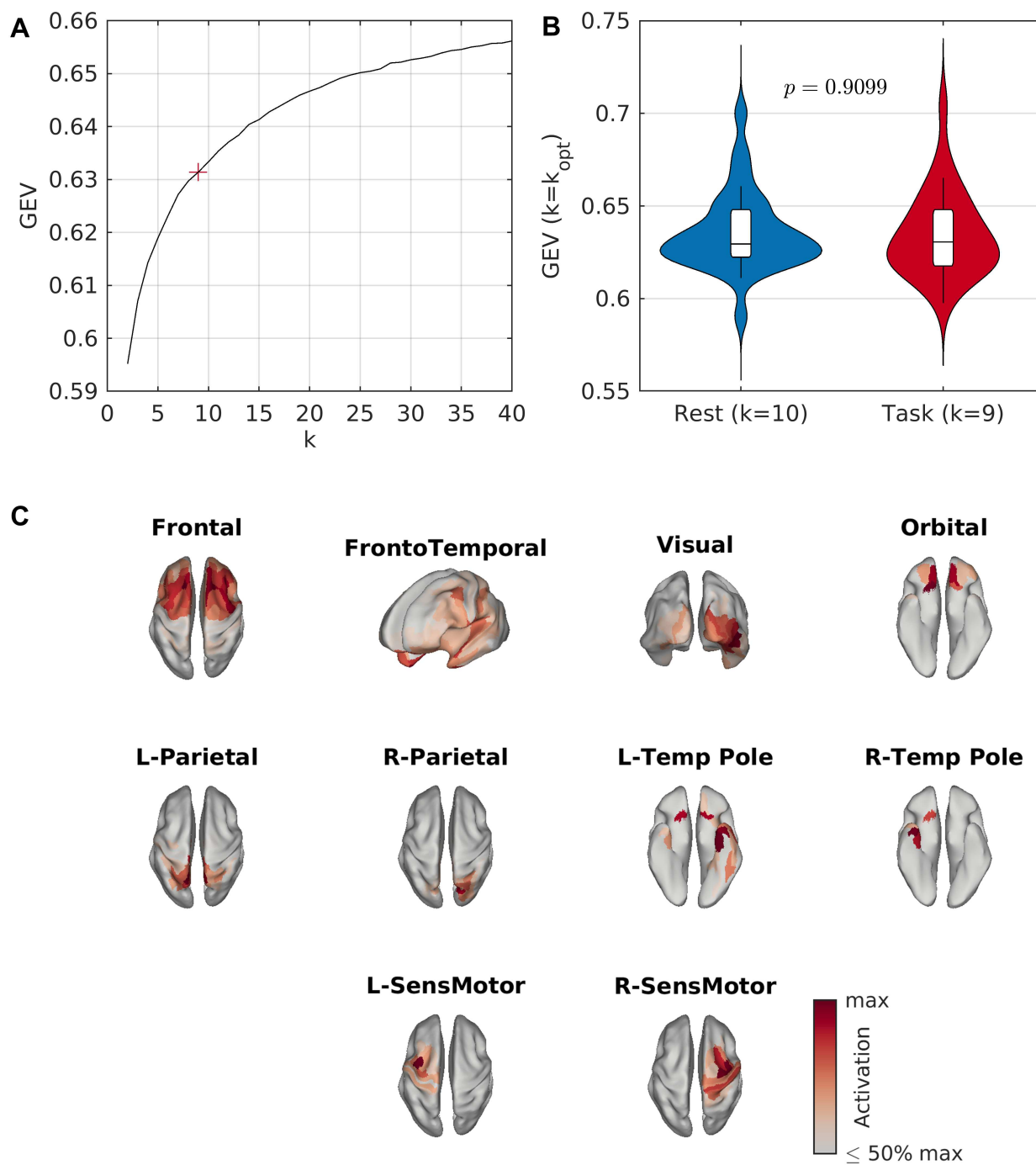


Figure 5: **Auditory task microstates.** (A) GEV vs number of states (k) for resting-state data. Here, GEV is calculated across the 150,000 peaks used for clustering. The kneedle algorithm found that $k = 10$ states was optimum, marked by a red '+'. (B) GEV across the full MEG scans, for $k = 10$. Distributions are shown across participants. Only GFP peaks from scan 1 for each participant were used for clustering, and hence scan 2 can be viewed as a replication/validation cohort. There is a small but significant decrease in GEV for scan 2. (C) Resting-state microstate maps derived from the k -means clustering algorithm for $k = 10$ states.

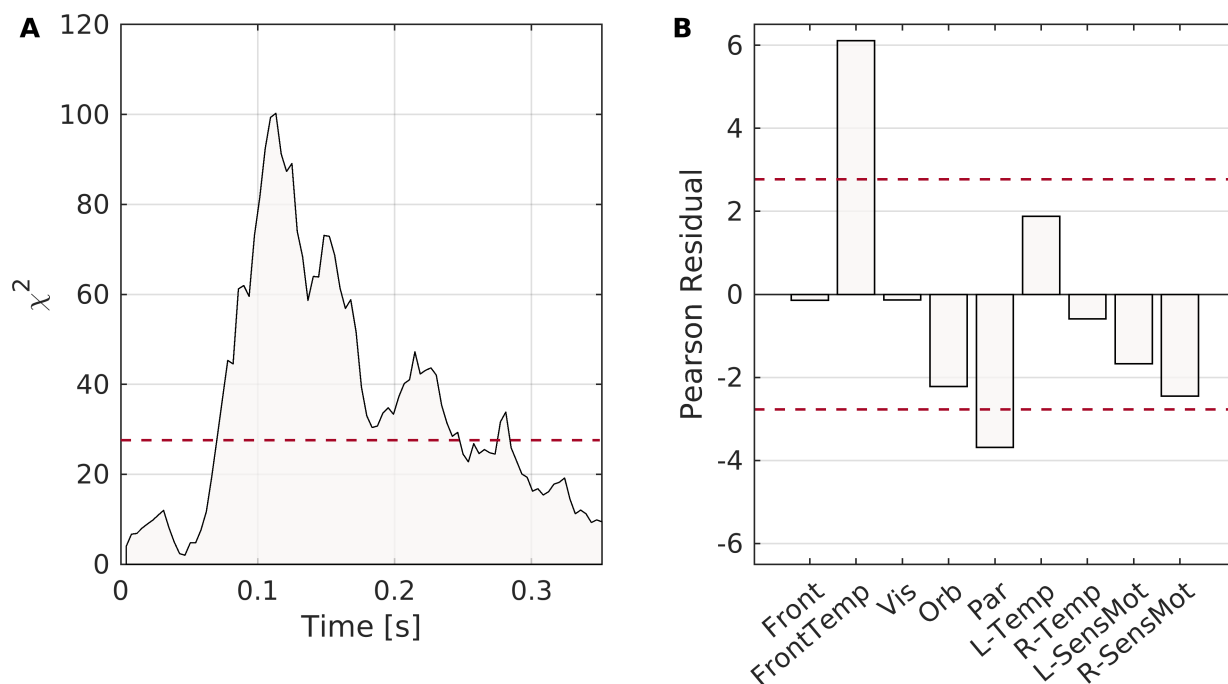


Figure 6: **Microstate response to auditory stimuli.** (A) χ^2 distance between observed and expected counts of each microstate vs time after stimulus. The peak response was 113 ms after the stimulus. (B) Pearson residuals for each state. For large sample sizes, under the null hypothesis the Pearson residual is approximately normally distributed. Here, Pearson residuals are averaged across all samples around the peak with a value of χ^2 greater than one-half the peak value. For both plots, dotted red lines show the Bonferroni corrected 95% significance level. Hence, these results suggest that between 70-280 ms following the stimulus the microstate response is significantly different that expected, due to a significantly increased likelihood of the frontotemporal state and decreased likelihood of the parietal state.

376 the validity and robustness of source-space MEG microstates. Using a k -means clustering algorithm, we showed
377 that 10 microstates can be reliably estimated from resting-state MEG data, and their spatial distributions are
378 similar to those quantified from task-based data. Source-space MEG microstates vary in their statistics such as
379 coverage and occurrence probabilities, and are associated with distinct functional connectivity signatures. These
380 results support the use of MEG microstates to understand dynamic functional connectivity during rest and task.

381 Interestingly, in resting-state data we observed the optimum number of states to be 10, explaining approxi-
382 mately 63% of the variance of the data. In resting-state sensor EEG, only four microstates have repeatedly been
383 reproduced and observed to be the optimum, explaining approximate 60-85% of variance in the data⁵. There are
384 a number of potential explanations for the differences between these results. One possible explanation is that
385 EEG usually has lower spatial resolution than MEG, due to (typically) fewer sensors and a blurring of the elec-
386 tric field by the skull tissue. In a study with high-density EEG (204 electrodes), seven maps were optimum⁵⁰,
387 supporting the hypothesis of higher spatial resolution potentially increasing the optimum number of maps. An-
388 other possible explanation is the criterion used for selecting the optimum number of maps, as many criteria are
389 available in the literature⁵. Discussion of this point, including motivation for our choice of criterion, are given in
390 Supplementary Text S1.2. The larger number of states in this study may also be due to performing clustering
391 in source space as opposed to sensor space. There is a non-uniform distribution of signal-to-noise ratio (SNR)
392 in the forward projection of the source dynamics to sensor space, and hence it is possible that states originat-
393 ing from low-SNR areas of the cortex or may be under-represented in the sensor space maps. Additionally, due
394 to finite spatial sampling of M/EEG sensors, multiple source topographies may result in non-unique maps, and
395 therefore multiple source-space states may appear similar at the sensor level. Both of these effects potentially
396 result in under-estimation of the number of states at the sensor level. In HMM studies of source-reconstructed
397 resting-state MEG, Baker et al.⁸ studied eight states while Vidaurre et al.¹² found twelve to be optimum, while
398 fMRI results have suggested ten reproducible resting-state networks⁷ or 7-8 states based on k -means cluster-
399 ing of dynamic resting-state functional connectivity patterns²¹, in line with our results demonstrating greater than
400 four states at the cortical level.

401 The ten resting-state microstates included four bilateral networks and three pairs of symmetric lateralized net-
402 works (Figure 2). The cognitive relevance of these microstates should be a focus of future work. One approach
403 to uncover the associations between microstates and cognition is to quantitatively compare microstate statistics
404 between cognitive states. Such approaches have widely been performed in the sensor-space EEG microstate
405 literature to gain insight into the functional significance of brain microstates^{13-16;18}, and the work presented here
406 opens new pathways to gain deeper anatomical insight at the cortical level. Here, we demonstrated that statis-
407 tics of our source-space cortical microstates differed between rest and a passive auditory mismatch paradigm
408 (Figure 5-6). We found hyperactivity of the frontotemporal microstate, which includes the auditory cortex, approx-

imately 100ms following an auditory stimulus. Interestingly, the well-studied auditory evoked response has been localized to the the auditory cortex and first peaks around 100ms following the stimulus⁹³, known as the N100 response, in line with our microstate results. Future work should build upon these approaches to examine the functional significance of these states.

A complementary approach is to uncover associations between microstates and the well studied resting-state networks (RSNs) widely studied in fMRI, which have been associated with cognitive domains in large cohort studies⁷. In sensor-space EEG, studies have demonstrated associations between microstates and fMRI-RSNS through convolution of the microstate time courses with a haemodynamic response function and general linear modelling^{34–36;38–40;68}, or through correlations between RSNs and microstate statistics³⁷. An advantage of working in source space for this purpose is that spatial patterns of microstate activations can be associated with RSNs when directly comparable brain atlases are used for parcellation of the brain dynamics in the M/EEG and fMRI data.

While the activation patterns of our microstates did not directly correspond to the well known resting-state networks (RSNs) often reported in fMRI studies⁷, interesting insight into this relationship could be gained by studying spatial patterns of synchrony associated with each microstate. Through the use of machine learning - specifically MVPA⁷⁷ - we found a significant association between active microstate class and cortical patterns of phase synchronization (Figure 4, Table 3). The spatial patterns of synchrony did not directly reflect the associated microstate maps, and the functional connectivity patterns identified here may give insight into the relationship between microstates and RSNs. A key example is the default mode network, which contains the medial/orbital frontal, medial parietal, and lateral parietal regions⁷. No single microstate had an activation pattern containing all of these ROIs, yet phase-locking patterns indicted microstates demonstraing medial/orbital frontal to medial parietal connectivity and medial parietal to lateral parietal connectivity (Figure 4B). Future work should involve simultaneous high-density source-reconstructed EEG and fMRI to study the relationship between source-space microstates and RSNs.

The microstate connectivity approach presented here also has potential as an alternative approach for studying dynamic functional connectivity. A typical approach for dynamic functional connectivity in the current literature is the use of a sliding window^{24–28}, which is limited by the arbitrary choice of window size meaning development of novel methods beyond the sliding window are crucial¹⁰. Our MVPA analysis indicated that windowing via microstate labelling and concatenation of samples within a state (i.e. microstate-segmented functional connectivity^{73;74}) is a powerful option for the study of dynamic functional connectivity states at a fast time scale without setting an *a priori* window length. However, this approach has some limitations. While MVPA classification was significant for all frequency bands, accuracy was not perfect and there may be overlaps between functional connectivity patterns of lateralized states (Figure 4). A second limitation of this approach is that it relies on the

442 assumption of a discrete number of functional connectivity states. While this assumption does not apply in gen-
443 eral to sliding-window connectivity studies, common subsequent analyses such as clustering networks^{21;26;29;30}
444 or recurrence analysis²⁸ make similar assumptions, and hence microstate-windowing can be viewed as an alter-
445 native to these approaches without the reliance on window length.

446 In recent years several alternative methodologies have been proposed for source-space brain state estima-
447 tion based on Hidden Markov Models (HMMs)^{8;11;12;88;94}. The use of a microstate pipeline instead of HMMs in
448 this study was motivated by evidence suggesting that for electrophysiological resting-state data, the underpin-
449 ning assumptions of HMMs for brain states are not always met. Koenig and Brandeis⁶³ highlighted that HMMs
450 cannot capture the empirical relationship between GFP and state stability, while Gschwind et al.³¹ discussed the
451 importance of long-range dependencies in the microstate sequence which are not accounted for by HMMs. Con-
452 versely, the source-space microstate pipeline presented here is based on data-driven clustering and hence does
453 not rely on many specific assumptions to be met - a detailed discussion of the assumptions and their justifica-
454 tion for electrophysiological data is given by Michel and Koenig⁵ - and hence may be more applicable to a wider
455 range of datasets. This was demonstrated by our simulations. Simulated data was generated through stimulation
456 of neural mass models, with stimulation patterns following a non-Markovian sequence. Hence, our biophysically
457 informed model did not meet the assumptions of the HMM. In these simulations, we found the microstate pipeline
458 greatly outperformed the HMM approach in terms of estimate the ground truth maps and brain-state sequences
459 (Figure 1). It should however be highlighted that the mechanisms underpinning the physiological origins of mi-
460 crostates in the human brain are currently not well understood and may not be reflected by our simulations, so
461 these results should not be interpreted as evidence that HMMs perform poorly for real resting-state brain data.
462 Future work should include simulations under a range of models and assumptions and a deeper analysis of var-
463 ious task-related data sets in order to perform a more detailed comparison between clustering approaches and
464 identify the correct circumstances under which each approach should be used.

465 4.1 Conclusions

466 We have presented a source-space microstate pipeline for estimating electrophysiological brain states. We
467 uncovered ten resting microstates which were associated with distinct patterns of activation and phase synchrony
468 across the cortex, and demonstrated these microstates were the result of stable non-stationary states arising as
469 opposed to random fluctuations in a stationary process. The microstates were associated with cognitive state;
470 in particular the resulting microstate probabilities were altered as a response to auditory stimulus, driven by
471 hyperactivity of the frontotemporal microstate. Our results suggest the methodology presented here is a powerful
472 tool for studying anatomically interpretable brain states and dynamic functional connectivity at the millisecond
473 scale.

References

- [1] M.P. van den Heuvel and H.E. Hulshoff Pol. Exploring the brain network: A review on resting state fMRI functional connectivity. *Eur Neuropsychopharmacol*, 20(8):519–534, 2010.
- [2] L. Douw, M.M. Schoonheim, D. Landi, M.L. van der Meer, J.J.G. Geurts, J.C. Reijneveld, M. Klein, and C.J. Stam. Cognition is related to resting-state small-world network topology: an megnetoencephalographic study. *Neuroscience*, 175:169–177, 2011. doi: [10.1016/j.neuroscience.2010.11.039](https://doi.org/10.1016/j.neuroscience.2010.11.039).
- [3] C. Babiloni, R. Lizio, N. Marzano, P. Capotosto, A. Soricelli, A.I. Triggiani, S. Cordone, L. Gesualdo, and C. Del Percio. Brain neural synchronization and functional coupling in alzheimer’s disease as revealed by resting state EEG rhythms. *Int J Psychophysiol*, 103:88–102, 2016. doi: [10.1016/j.ijpsycho.2015.02.008](https://doi.org/10.1016/j.ijpsycho.2015.02.008).
- [4] J.R. Cohen. The behavioural and cognitive relevance of time-varying, dynamic changes in functional connectivity. *NeuroImage*, 180:515–525, 2018. doi: [10.1016/j.neuroimage.2017.09.036](https://doi.org/10.1016/j.neuroimage.2017.09.036).
- [5] C.M. Michel and T. Koenig. EEG microstates as a tool for studying the temporal dynamics of whole-brain neuronal networks: A review. *NeuroImage*, 180(B):577–593, 2018. doi: [10.1016/j.neuroimage.2017.11.062](https://doi.org/10.1016/j.neuroimage.2017.11.062).
- [6] W.H. Lee, D.A. Moser, G.E. Ing, A. Doucet, and S. Frangou. Behavioural and health correlates of resting-state metastability in the human connectome project. *Brain Topogr*, 32:80–86, 2019. doi: [P10.1007/s10548-018-0672-5](https://doi.org/10.1007/s10548-018-0672-5).
- [7] S.M. Smith, P.T. Fox, K.L. Miller, D.C. Glahn, P.M. Fox, C.E. Mackay, N. Filippini, K.E. Watkins, R. Toro, A.R. Laird, and C.F. Beckmann. Correspondence of the brain’s functional architecture during activation and rest. *Proc Natl Acad Sci USA*, 106(31):13040–13045, 2009. doi: [10.1073/pnas.0905267106](https://doi.org/10.1073/pnas.0905267106).
- [8] A.P. Baker, M.J. Brookes, S.M. Smith, T. Behrens, P.J. Probert Smith, and M. Woolrich. Fast transient networks in spontaneous human brain activity. *eLife*, 3:e01867, 2014. doi: [10.7554/eLife.01867](https://doi.org/10.7554/eLife.01867).
- [9] A. Khanna, A. Pascual-Leone, C.M. Michel, and F. Farzan. Microstates in resting-state EEG: Current status and future directions. *Neurosci Biobehav Rev*, 49:105–113, 2015. doi: [10.1016/j.neubiorev.2014.12.010](https://doi.org/10.1016/j.neubiorev.2014.12.010).
- [10] G.C. O’Neill, P. Tewarie, D. Vidaurre, L. Liuzzi, M.W. Woolrich, and M.J. Brookes. Dynamics of large-scale electrophysiological networks: A technical review. *NeuroImage*, 180(B):559–576, 2018. doi: [10.1016/j.neuroimage.2017.10.003](https://doi.org/10.1016/j.neuroimage.2017.10.003).
- [11] J. Taghia, W. Cai, S. Ryali, J. Kockalka, J. Nicholas, T. Chen, and M. Vinod. Uncovering hidden brain state dynamics that regulate performance and decision making during cognition. *Nat Commun*, 9:2505, 2018. doi: [10.1038/s41467-018-04723-6](https://doi.org/10.1038/s41467-018-04723-6).
- [12] D. Vidaurre, L.T. Hunt, A.J. Quinn, B.A.E. Hunt, M.J. Brookes, A.C. Nobre, and M.W. Woolrich. Spontaneous cortical activity transiently organises into frequency specific phase-coupling networks. *Nat Commun*, 9:2987, 2018. doi: [10.1038/s41467-018-05316-z](https://doi.org/10.1038/s41467-018-05316-z).
- [13] V. Brodbeck, A. Kuhn, F. von Wegner, A. Morzelewski, E. Tagliazucchi, S. Borisov, C.M. Michel, and H. Laufs. EEG microstates of wakefulness and NREM sleep. *NeuroImage*, 62(3):2129–2139, 2012. doi: [10.1016/j.neuroimage.2012.05.060](https://doi.org/10.1016/j.neuroimage.2012.05.060).
- [14] J. Britz, L.D. Hernández, T. Ro, and C.M. Michel. EEG-microstate dependent emergence of perceptual awareness. *Front Behav Neurosci*, 8:163, 2014. doi: [10.3389/fnbeh.2014.00163](https://doi.org/10.3389/fnbeh.2014.00163).
- [15] P. Milz, P.L. Faber, D. Lehmann, T. Koenig, K. Kochi, and R.D. Pascual-Marqui. The functional significance of EEG microstates - associations with modalities of thinking. *NeuroImage*, 125:643–656, 2016. doi: [10.1016/j.neuroimage.2015.08.023](https://doi.org/10.1016/j.neuroimage.2015.08.023).
- [16] B.A. Seitzman, M. Abell, S.C. Bartley, M.A. Erickson, A.R. Bolbecker, and W.P. Hetrick. Cognitive manipulation of brain electric microstates. *NeuroImage*, 146:533–543, 2017. doi: [10.1016/j.neuroimage.2016.10.002](https://doi.org/10.1016/j.neuroimage.2016.10.002).
- [17] R. Liégeois, J. Li, R. Kong, C. Orban, D. Van De Ville, T. Ge, M.R. Sabuncu, and B.T.T. Yeo. Resting brain dynamics at different timescales capture distinct aspects of human behaviour. *Nat Commun*, 10:2317, 2019. doi: [10.1038/s41467-019-10317-7](https://doi.org/10.1038/s41467-019-10317-7).
- [18] F. Zappasodi, M.G. Perrucci, A. Saggino, P. Croce, P. Mercuri, R. Romanelli, R. Colom, and S.J.H. Ebisch. EEG microstates distinguish between cognitive components of fluid reasoning. *NeuroImage*, 189:560–573, 2019. doi: [10.1016/j.neuroimage.2019.01.067](https://doi.org/10.1016/j.neuroimage.2019.01.067).

- 520 [19] Q. Zhou, L. Zhang, J. Feng, and C.Y. Zac Lo. Tracking the main states of dynamic functional connectivity in resting
521 state. *Front Neurosci*, 13:685, 2019. doi: [10.3389/fnins.2019.00685](https://doi.org/10.3389/fnins.2019.00685).
- 522 [20] C.F. Beckmann, M. DeLuca, J.T. Devlin, and S.M. Smith. Investigations into resting-state connectivity using indepen-
523 dent component analysis. *Phil Trans R Soc B*, 360:1001–1013, 2005. doi: [10.1098/rstb.2005.1634](https://doi.org/10.1098/rstb.2005.1634).
- 524 [21] E.A. Allen, E. Damaraju, S.M. Plis, E.B. Erhardt, T. Eichele, and V.D. Calhoun. Tracking whole-brain connectivity
525 dynamics in the resting state. *Cereb Cortex*, 24(3):663–676, 2014. doi: [10.1093/cercor/bhs352](https://doi.org/10.1093/cercor/bhs352).
- 526 [22] M.J. Brookes, M. Woolrich, H. Luckhoo, D. Price, J.R. Hale, M.C. Stephenson, G.R. Barnes, S.M. Smith, and P.G.
527 Morris. Investigating the electrophysiological basis of resting state networks using magnetoencephalography. *Proc
528 Natl Acad Sci*, 108(40):16783–16788, 2011. doi: [10.1073/pnas.1112685108](https://doi.org/10.1073/pnas.1112685108).
- 529 [23] Q. Liu, S. Farahibozorg, C. Porcaro, N. Wenderoth, and D. Mantini. Detecting large-scale networks in the human brain
530 using high-density electroencephalography. *Hum Brain Mapp*, 38:4631–4643, 2017. doi: [10.1002/hbm.23688](https://doi.org/10.1002/hbm.23688).
- 531 [24] F. de Pasquale, S. Della Penna, A.Z. Snyder, C. Lewis, D. Mantini, L. Marzetti, P. Belardinelli, L. Ciancetta, V. Pizzella,
532 G.L. Romani, and M. Corbetta. Temporal dynamics of spontaneous MEG activity in brain networks. *Proc Natl Acad
533 Sci USA*, 107(13):6040–6045, 2010. doi: [10.1073/pnas.0913863107](https://doi.org/10.1073/pnas.0913863107).
- 534 [25] M.J. Brookes, G.C. O’Neill, E.L. Hall, M.W. Woolrich, A. Baker, S.P. Corner, S.E. Robson, P.G. Morris, and G.R. Barnes.
535 Measuring temporal, spectral and spatial changes in electrophysiological brain network connectivity. *Neuroimage*, 91:
536 282–299, 2014. doi: [10.1016/j.neuroimage.2013.12.066](https://doi.org/10.1016/j.neuroimage.2013.12.066).
- 537 [26] G.C. O’Neill, M. Bauer, M.W. Woolrich, P.G. Morris, G.R. Barnes, and M.J. Brookes. Dynamic recruitment of resting
538 state sub-networks. *Neuroimage*, 115:85–95, 2015. doi: [10.1016/j.neuroimage.2015.04.030](https://doi.org/10.1016/j.neuroimage.2015.04.030).
- 539 [27] F. de Pasquale, S. Della Penna, O. Sporns, G.L. Romani, and M. Corbetta. A dynamic core network and global
540 efficiency in the resting human brain. *Cereb Cortex*, 26(10):4015–4033, 2016. doi: [10.1093/cercor/bhv185](https://doi.org/10.1093/cercor/bhv185).
- 541 [28] M.A. Lopes, J. Zhang, D. Krzemiński, K. Hamandi, Q. Chen, L. Livi, and N. Masuda. Recurrence quantification analysis
542 of dynamic brain networks. *Eur J Neurosci*, 2020. doi: [10.1111/ejn.14960](https://doi.org/10.1111/ejn.14960).
- 543 [29] A. Mheich, M. Hassan, M. Khalil, C. Berrou, and F. Wendling. A new algorithm for spatiotemporal analysis of brain
544 functional connectivity. *J Neurosci Methods*, 242:77–81, 2015. doi: [10.1016/j.jneumeth.2015.01.002](https://doi.org/10.1016/j.jneumeth.2015.01.002).
- 545 [30] M. Hassan, P. Benquet, A. Biraben, C. Berrou, O. Dufor, and F. Wendling. Dynamic reorganization of functional brain
546 networks during picture naming. *Cortex*, 74:276–288, 2015. doi: [10.1016/j.cortex.2015.08.019](https://doi.org/10.1016/j.cortex.2015.08.019).
- 547 [31] M. Gschwind, C.M. Michel, and D. Van De Ville. Long-range dependencies make the difference - com-
548 ment on “a stochastic model for EEG microstate sequence analysis”. *Neuroimage*, 117:449–455, 2015. doi:
549 [10.1016/j.neuroimage.2015.05.062](https://doi.org/10.1016/j.neuroimage.2015.05.062).
- 550 [32] A. Khanna, A. Pascual-Leone, and F. Farzan. Reliability of resting-state microstate features in electroencephalography.
551 *PLoS One*, 9(12):e114163, 2014. doi: [10.1371/journal.pone.0114163](https://doi.org/10.1371/journal.pone.0114163).
- 552 [33] F. von Wegner, P. Knaut, and H. Laufs. EEG microstate sequences from different clustering algorithms are information-
553 theoretically invariant. *Front Comput Neurosci*, 12:70, 2018. doi: [10.3389/fncom.2018.00070](https://doi.org/10.3389/fncom.2018.00070).
- 554 [34] J. Britz, D. Van De Ville, and C.M. Michel. BOLD correlates of EEG topography reveal rapid resting-state network
555 dynamics. *Neuroimage*, 52(4):1162–1170, 2010. doi: [10.1016/j.neuroimage.2010.02.052](https://doi.org/10.1016/j.neuroimage.2010.02.052).
- 556 [35] F. Musso, J. Brinkmeyer, A. Mobascher, T. Warbrick, and G. Winterer. Spontaneous brain activity and EEG microstates.
557 a novel EEG/fMRI analysis approach to explore resting-state networks. *Neuroimage*, 52:1149–1161, 2010. doi:
558 [10.1016/j.neuroimage.2010.01.093](https://doi.org/10.1016/j.neuroimage.2010.01.093).
- 559 [36] H. Yuan, V. Zotev, R. Phillipis, W.C. Drevets, and J. Bodurka. Spatiotemporal dynamics of the brain at rest - exploring
560 EEG microstates as electrophysiological signatures of BOLD resting state networks. *Neuroimage*, 60:2062–2072,
561 2012. doi: [10.1016/j.neuroimage.2012.02.031](https://doi.org/10.1016/j.neuroimage.2012.02.031).
- 562 [37] J. Schumacher, L.R. Peraza, M. Firbank, A.J. Thomas, M. Kaiser, P. Gallagher, J.T. O’Brien, A.M. Blamire, and J.P.
563 Taylor. Dysfunctional brain dynamics and their origin in lewy body dementia. *Brain*, 142(6):1767–1782, 2019. doi:
564 [10.1093/brain/awz069](https://doi.org/10.1093/brain/awz069).
- 565 [38] R. Abreu, J. Jorge, A. Leal, T. Koenig, and P. Figueiredo. EEG microstates predict concurrent fMRI dynamic functional
566 connectivity states. *Brain Topogr*, 2020. doi: [10.1007/s10548-020-00805-1](https://doi.org/10.1007/s10548-020-00805-1).

- 567 [39] J. Xu, Y. Pan, S. Zhou, G. Zou, J. Liu, Z. Su, Q. Zou, and J.H. Gao. EEG microstates are correlated with brain functional
568 networks during slow-wave sleep. *Neuroimage*, 215:116786, 2020. doi: [10.1016/j.neuroimage.2020.116786](https://doi.org/10.1016/j.neuroimage.2020.116786).
- 569 [40] O.A. Zoubi, M. Misaki, A. Tsuchiyagaito, A. Mayeli, V. Zotev, Tulsa 1000 Investigators, H. Refai, M. Paulus, and J. Bo-
570 durka. Canonical EEG microstate dynamic properties and their associations with fMRI signals at resting brain. *bioRxiv*,
571 page 2020.08.14.251066, 2020. doi: [10.1101/2020.08.14.251066](https://doi.org/10.1101/2020.08.14.251066).
- 572 [41] D. Lehmann. Brain electric microstates and cognition: The atoms of thought. 1990. doi: [10.1007/978-1-4757-1083-
573 0_10](https://doi.org/10.1007/978-1-4757-1083-0_10).
- 574 [42] K. Nishida, Y. Morishima, M. Yoshimura, T. Isotani, S. Irisawa, J. Jann, T. Dierks, W. Strik, T. Kinoshita, and T. Koenig.
575 EEG microstates associated with salience and frontoparietal networks in frontotemporal dementia, schizophrenia and
576 Alzheimer's disease. *Clin Neurophysiol*, 124(6):1106–1114, 2013. doi: [10.1016/j.clinph.2013.01.005](https://doi.org/10.1016/j.clinph.2013.01.005).
- 577 [43] C.S. Musaeus, M.S. Nielsen, and P. Høgh. Microstates as disease and progression markers in patients with mild
578 cognitive impairment. *Front Neurosci*, 13:563, 2019. doi: [10.3389/fnins.2019.00563](https://doi.org/10.3389/fnins.2019.00563).
- 579 [44] U. Smailovic, T. Koenig, E.J. Laukka, G. Kalpouzos, T. Andersson, B. Winblad, and V. Jelic. EEG time signa-
580 ture in Alzheimer's disease: Functional brain networks falling apart. *Neuroimage Clin*, 24:102046, 2019. doi:
581 [10.1016/j.nicl.2019.102046](https://doi.org/10.1016/j.nicl.2019.102046).
- 582 [45] L. Tait, F. Tamagnini, G. Stothart, E. Barvas, C. Monaldini, R. Frusciante, M. Volpini, S. Guttman, E. Coulthard, J.T.
583 Brown, N. Kazanina, and M. Goodfellow. EEG microstate complexity for aiding early diagnosis of Alzheimer's disease.
584 *Sci Rep*, 10:17627, 2020. doi: [10.1038/s41598-020-74790-7](https://doi.org/10.1038/s41598-020-74790-7).
- 585 [46] D. Lehmann, P.L. Faber, S. Galderisi, W.M. Herrmann, T. Kinoshita, M. Koukkou, A. Mucci, R.D. Pascual-Marqui,
586 N. Saito, J. Wackermann, G. Winterer, and T. Koenig. EEG microstate duration and syntax in acute, medication-
587 naïve, first-episode schizophrenia: a multi-center study. *Psychiatry Res Neuroimaging*, 138(2):141–156, 2005. doi:
588 [10.1016/j.pscychresns.2004.05.007](https://doi.org/10.1016/j.pscychresns.2004.05.007).
- 589 [47] C. Andreou, P.L. Faber, G. Leicht, D. Schoettle, N. Polomac, I.L. Hanganu-Opatz, D. Lehmann, and C. Mulert. Resting-
590 state connectivity in the prodromal phase of schizophrenia: insights from eeg microstates. *Schizophr Res*, 152(2-3):
591 513–20, 2014. doi: [10.1016/j.schres.2013.12.008](https://doi.org/10.1016/j.schres.2013.12.008).
- 592 [48] M.I. Tomescu, T.A. Rihs, R. Becker, J. Britz, A. Custo, F. Grouiller, M. Schneider, M. Debbané, S. Eliez, and C.M.
593 Michel. Deviant dynamics of EEG resting state pattern in 22q11.2 deletion syndrome adolescents: A vulnerability
594 marker of schizophrenia? *Schizophr Res*, 157(1-3):175–81, 2014. doi: [10.1016/j.schres.2014.05.036](https://doi.org/10.1016/j.schres.2014.05.036).
- 595 [49] A. Custo, S. Vulliemoz, F. Grouiller, D. Van De Ville, and C. Michel. EEG source imaging of brain states using spa-
596 tiotemporal regression. *Neuroimage*, (96):106–116, 2014. doi: [10.1016/j.neuroimage.2014.04.002](https://doi.org/10.1016/j.neuroimage.2014.04.002).
- 597 [50] A. Custo, D. Van De Ville, W.M. Wells, M.I. Tomescu, D. Brunet, and C.M. Michel. Electroencephalographic resting-
598 state networks: Source localization of microstates. *Brain Conn*, 7(10):671–682, 2017. doi: [10.1089/brain.2016.0476](https://doi.org/10.1089/brain.2016.0476).
- 599 [51] R.D. Pascual-Marqui, D. Legmann, P. Faber, P. Milz, K. Kochi, M. Yoshimura, K. Nishida, T. Isotani, and T. Kinoshita.
600 The resting microstate networks (RMN): cortical distributions, dynamics, and frequency specific information flow. *arXiv*,
601 page 1411.1949, 2014.
- 602 [52] P. Milz, R.D. Pascual-Marqui, P. Achermann, K. Kochi, and P.L. Faber. The EEG microstate topography is
603 predominantly determined by intracortical sources in the alpha band. *Neuroimage*, 162:353–361, 2017. doi:
604 [10.1016/j.neuroimage.2017.08.058](https://doi.org/10.1016/j.neuroimage.2017.08.058).
- 605 [53] J.D. Kropotov. Alpha rhythms. In J.D. Kropotov, editor, *Quantitative EEG, Event-Related Potentials and Neurotherapy*,
606 pages 29–58. Academic Press, San Diego, 2009. ISBN 978-0-12-374512-5. doi: [10.1016/B978-0-12-374512-5.00002-
607 5](https://doi.org/10.1016/B978-0-12-374512-5.00002-5).
- 608 [54] D.M. Goldenholz, S.P. Ahlfors, M.S. Hämäläinen, D. Sharon, M. Ishitobi, L.M. Vaina, and S.M. Stufflebeam. Mapping
609 the signal-to-noise-ratios of cortical sources in magnetioenceopahlography and electroencephalography. *Hum Brain
610 Mapp*, 30(3):1077–1086, 2009. doi: [10.1002/hbm.20571](https://doi.org/10.1002/hbm.20571).
- 611 [55] R.D. Pascual-Marqui, C.M. Michel, and D. Lehmann. Segmentation of brain electrical activity into microstates: model
612 estimation and validation. *IEEE Trans Biomed Eng*, 42(7):658–665, 1995. doi: [10.1109/10.391164](https://doi.org/10.1109/10.391164).
- 613 [56] T. Koenig, D. Lehmann, M.C.G. Merlo, K. Kochi, Hell D., and Koukkou M. A deviant EEG brain microstate in
614 acute, neuroleptic-naïve schizophrenics at rest. *Eur Arch Psychiatry Clin Neurosci*, 249:205–211, 1999. doi:
615 [10.1007/s004060050088](https://doi.org/10.1007/s004060050088).

- 616 [57] F. von Wegner, S. Bauer, F. Rosenow, J. Triesch, and H. Laufs. EEG microstate periodicity explained by rotating phase
617 patterns of resting-state alpha oscillations. *Neuroimage*, 224:117372, 2021. doi: [10.1016/j.neuroimage.2020.117372](https://doi.org/10.1016/j.neuroimage.2020.117372).
- 618 [58] L. Tait, A. Özkan, M.J. Szul, and J. Zhang. Cortical source imaging of resting-state meg with a high resolution atlas:
619 An evaluation of methods. *bioRxiv*, page 2020.01.12.903302, 2020. doi: [10.1101/2020.01.12.903302](https://doi.org/10.1101/2020.01.12.903302).
- 620 [59] R.D. Pascual-Marqui. Discrete, 3D distributed, linear imaging methods of electric neuronal activity. Part 1: exact, zero
621 error localization. *arXiv:0710.3341 [math-ph]*, 2007. URL <http://arxiv.org/pdf/0710.3341>.
- 622 [60] R.D. Pascual-Marqui. Theory of the EEG inverse problem. In S. Tong and N. Thakor, editors, *Quantitative EEG*
623 *analysis: methods and clinical applications*, pages 121–140. Artech House, Boston, 2009.
- 624 [61] M.F. Glasser, T.S. Coalson, E.C. Robinson, C.D. Hacker, J. Harwell, E. Yacoub, K. Ugurbil, J. Andersson, C.F. Beck-
625 mann, M. Jenkinson, S.M. Smith, and D.C. Van Essen. A multi-modal parcellation of human cerebral cortex. *Nature*,
626 536(7615):171–178, 2016. doi: [10.1038/nature18933](https://doi.org/10.1038/nature18933).
- 627 [62] C.M. Michel, T. Koenig, and D. Brandeis. Electrical neuroimaging in the time domain. In C.M. Michel, T. Koenig,
628 D. Brandeis, L.R.R. Gianotti, and J. Wackermann, editors, *Electrical Neuroimaging*, pages 111–143. Cambridge Uni-
629 versity Press, 2009.
- 630 [63] T. Koenig and D. Brandeis. Inappropriate assumptions about EEG state changes and their impact on the quantification
631 of EEG state dynamics. *Neuroimage*, 125:1104–1106, 2016. doi: [10.1016/j.neuroimage.2015.06.035](https://doi.org/10.1016/j.neuroimage.2015.06.035).
- 632 [64] D. Arthur and S. Vassilvitskii. K-means++: The advantages of careful seeding. In *Discrete Algorithms: SODA-07*
633 *Proceedings of the Eighteenth Annual ACM-SIAM Symposium*, page 1027–1035, 2007.
- 634 [65] M.M. Murray, D. Brunet, and C.M. Michel. Topographic ERP analyses: A step-by-step tutorial review. *Brain Topogr*, 20:
635 249–264, 2008. doi: [10.1007/s10548-008-0054-5](https://doi.org/10.1007/s10548-008-0054-5).
- 636 [66] V. Satopää, J. Albrecht, D. Irwin, and B. Raghavan. Finding a “kneedle” in a haystack: Detecting knee points in system
637 behavior. In *2011 31st International Conference on Distributed Computing Systems Workshops*, pages 166–171, 2011.
638 doi: [10.1109/ICDCSW.2011.20](https://doi.org/10.1109/ICDCSW.2011.20).
- 639 [67] T. Koenig, L. Prichep, D. Lehmann, P. Valdes Sosa, E. Braeker, H. Kleinlogel, R. Isenhardt, and E.R. John. Millisecond
640 by millisecond, year by year: Normative EEG microstates and developmental stages. *NeuroImage*, 16(1):41–48, 2002.
641 doi: [10.1006/nimg.2002.1070](https://doi.org/10.1006/nimg.2002.1070).
- 642 [68] D. Van De Ville, J. Britz, and C.M. Michel. EEG microstate sequences in healthy humans at rest reveal scale-free
643 dynamics. *Proc Natl Acad Sci USA*, 107(42):18179–18184, 2010. doi: [10.1073/pnas.1007841107](https://doi.org/10.1073/pnas.1007841107).
- 644 [69] A. Lempel and J. Ziv. On the complexity of finite sequences. *IEEE Trans. Inf. Theory*, 22:75–81, 1976. doi:
645 [10.1109/TIT.1976.1055501](https://doi.org/10.1109/TIT.1976.1055501).
- 646 [70] Xiaoku Liu, Chunlai Zhang, Zheng Ji, Yi Ma, Xiaoming Shang, Qi Zhang, Wencheng Zheng, Xia Li, Jun Gao, Ruofan
647 Wang, Jiang Wang, and Haitao Yu. Multiple characteristics analysis of Alzheimer’s electroencephalogram by power
648 spectral density and Lempel–Ziv complexity. *Cogn Neurodyn*, 10:121–133, 2016. doi: [10.1007/s11571-015-9367-8](https://doi.org/10.1007/s11571-015-9367-8).
- 649 [71] Y. Zhang, S. Wei, C. Di Maria, and C. Liu. Using Lempel–Ziv complexity to assess ECG signal quality. *J. Med. Biol.*
650 *Eng.*, 36:625–634, 2016. doi: [10.1007/s40846-016-0165-5](https://doi.org/10.1007/s40846-016-0165-5).
- 651 [72] F. von Wegner, E. Tagliazucchi, and H. Laufs. Information-theoretical analysis of resting state EEG mi-
652 crostate sequences - non-markovianity, non-stationarity and periodicities. *Neuroimage*, 158:99–111, 2017. doi:
653 [10.1016/j.neuroimage.2017.06.062](https://doi.org/10.1016/j.neuroimage.2017.06.062).
- 654 [73] F. Hatz, M. Hardmeier, N. Benz, M. Ehrensperger, U. Gschwandtner, S. Rüegg, C. Schindler, A.U. Monsch, and
655 P. Fuhr. Microstate connectivity alterations in patients with early Alzheimer’s disease. *Alz Res Therapy*, 7:78, 2015.
656 doi: [10.1186/s13195-015-0163-9](https://doi.org/10.1186/s13195-015-0163-9).
- 657 [74] F. Hatz, M. Hardmeier, H. Bousleiman, S. Rüegg, C. Schindler, and P. Fuhr. Reliability of functional connectivity of
658 electroencephalography applying microstate-segmented versus classical calculation of phase lag index. *Brain Conn*,
659 6(6):461–469, 2016. doi: [10.1089/brain.2015.0368](https://doi.org/10.1089/brain.2015.0368).
- 660 [75] M. Vinck, R. Oostenveld, M. van Wingerden, F. Battaglia, and C.M.A. Pennartz. An improved index of phase-
661 synchronization for electrophysiological data in the presence of volume-conduction, noise and sample-size bias. *Neu-*
662 *roimage*, 55(4):1548–1565, 2011. doi: [10.1016/j.neuroimage.2011.01.055](https://doi.org/10.1016/j.neuroimage.2011.01.055).

- 663 [76] G.L. Colclough, M.W. Woolrich, P.K. Tewarie, M.J. Brookes, A.J. Quinn, and S.M. Smith. How reliable are MEG resting-
664 state connectivity metrics? *Neuroimage*, 138:284–293, 2016. doi: [10.1016/j.neuroimage.2016.05.070](https://doi.org/10.1016/j.neuroimage.2016.05.070).
- 665 [77] M.S. Treder. MVPA-light: A classification and regression toolbox for multi-dimensional data. *Front Neurosci*, 14:289,
666 2020. doi: [10.3389/fnins.2020.00289](https://doi.org/10.3389/fnins.2020.00289).
- 667 [78] A Agresti. *Categorical Data Analysis*. John Wiley & Sons, 2012.
- 668 [79] J. Vrba and S.E. Robinson. Signal processing in magnetoencephalography. *Methods*, 25(2):249–271, 2001. doi:
669 [10.1006/meth.2001.1238](https://doi.org/10.1006/meth.2001.1238).
- 670 [80] R. Oostenveld, P. Fries, E. Maris, and J.M. Schoffelen. Fieldtrip: Open source software for advanced analysis of MEG,
671 EEG, and invasive electrophysiological data. *Comput Intell Neurosci*, 2011:156869, 2011. doi: [10.1155/2011/156869](https://doi.org/10.1155/2011/156869).
- 672 [81] A. Hyvarinen. Fast and robust fixed-point algorithms for independent component analysis. *IEEE Trans Neural Net*, 10
673 (3):626–634, 1999. doi: [10.1109/72.761722](https://doi.org/10.1109/72.761722).
- 674 [82] A.M. Dale, B. Fischl, and M.I. Sereno. Cortical surface-based analysis. I. segmentation and surface reconstruction.
675 *Neuroimage*, 9(2):179–94, 1999. doi: [10.1006/nimg.1998.0395](https://doi.org/10.1006/nimg.1998.0395).
- 676 [83] G. Nolte. The magnetic lead field theorem in the quasi-static approximation and its use for magnetoencephalography
677 forward calculation in realistic volume conductors. *Phys Med Biol*, 48(22):3637–3652, 2003. doi: [10.1099/0031-
678 9155/48/22/002](https://doi.org/10.1099/0031-9155/48/22/002).
- 679 [84] Q. Fang and D.A. Boas. Tetrahedral mesh generation from volumetric binary and grayscale images. *IEEE In-*
680 *ternational Symposium on Biomedical Imaging: From Nano to Macro*, 2009 ISBI '09:1142–1145, 2009. doi:
681 [10.1109/ISBI.2009.5193259](https://doi.org/10.1109/ISBI.2009.5193259).
- 682 [85] A.M. Dale, A.K. Liu, B.R. Fischl, R.L. Buckner, J.W. Beldic, J.D. Lewine, and E. Halgren. Dynamic statistical
683 parametric mapping: Combining fMRI and MEG for high-resolution imaging of cortical activity. *Neuron*, 26(1):55–67,
684 2000. doi: [10.1016/S0896-6273\(00\)81138-1](https://doi.org/10.1016/S0896-6273(00)81138-1).
- 685 [86] A. Hillebrand and G.R. Barnes. The use of anatomical constraints with MEG beamformers. *NeuroImage*, 20(4):
686 2302–2313, 2003. doi: [10.1016/j.neuroimage.2003.07.031](https://doi.org/10.1016/j.neuroimage.2003.07.031).
- 687 [87] A. Stolk, A. Todorovic, J.M. Schoffelen, and R. Oostenveld. Online and offline tools for head movement compensation in
688 MEG. *Neuroimage*, 68:38–48, 2013. doi: [10.1016/j.neuroimage.2012.11.047](https://doi.org/10.1016/j.neuroimage.2012.11.047).
- 689 [88] D. Vidaurre, A.J. Quinn, A.P. Baker, D. Dupret, A. Tejero-Cantero, and M.W. Woolrich. Spectrally resolved fast transient
690 brain states in electrophysiological data. *Neuroimage*, 126:81–95, 2016. doi: [10.1016/j.neuroimage.2015.11.047](https://doi.org/10.1016/j.neuroimage.2015.11.047).
- 691 [89] F. von Wegner, E. Tagliazucchi, V. Brodbeck, and H. Laufs. Analytical and empirical fluctuation functions of the
692 EEG microstate random walk - short-range vs. long-range correlations. *Neuroimage*, 141:442–451, 2016. doi:
693 [10.1016/j.neuroimage.2016.07.050](https://doi.org/10.1016/j.neuroimage.2016.07.050).
- 694 [90] G. Deco, V. Jirsa, A.R. McIntosh, O. Sporns, and R. Kötter. Key role of coupling, delay, and noise in resting brain
695 fluctuations. *Proc Natl Acad Sci USA*, 106(25):10302–10307, 2009. doi: [10.1073/pnas.0901831106](https://doi.org/10.1073/pnas.0901831106).
- 696 [91] R.G. Abeysuriya, J. Hadida, S.N. Sotiropoulos, S. Jbabdi, R. Becker, B.A.E. Hunt, M.J. Brookes, and M.W. Woolrich.
697 A biophysical model of dynamic balancing of excitation and inhibition in fast oscillatory large-scale networks. *PLoS
698 Comput Biol*, 14(2):e1006007, 2018. doi: [10.1371/journal.pcbi.1006007](https://doi.org/10.1371/journal.pcbi.1006007).
- 699 [92] L. Tait and J. Zhang. +microstate: A matlab toolbox for brain microstate analysis in sensor and cortical eeg/meg.
700 *bioRxiv*, page 2021.07.13.452193, 2021. doi: [10.1101/2021.07.13.452193](https://doi.org/10.1101/2021.07.13.452193).
- 701 [93] T.W. Picton. *Human Auditory Evoked Potentials*. Plural Publishing, Inc., San Diego, 2010.
- 702 [94] M. Gärtner, V. Brodbeck, H. Laufs, and G. Schneider. A stochastic model for eeg microstate sequence analysis.
703 *Neuroimage*, 104:199–208, 2015. doi: [10.1016/j.neuroimage.2014.10.014](https://doi.org/10.1016/j.neuroimage.2014.10.014).

Supplementary Files

This is a list of supplementary files associated with this preprint. Click to download.

- [Sourcemicrostatessupp.pdf](#)